# Global *SH*-wave propagation using a parallel axi-symmetric spherical finite-difference scheme: application to whole mantle scattering

Gunnar Jahnke[1,2], Michael S. Thorne[3], Alain Cochard[1,4], Heiner Igel[1]

[1]*Department of Earth and Environmental Sciences, Ludwig Maximilians Universität, Theresienstrasse 41, 80333 Munich, Germany.*
[2]*Now at: Federal Institute of Geosciences and Natural Resources, Stilleweg 2, 30655 Hanover, Germany.*
[3]*Department of Geology and Geophysics, University of Utah, Salt Lake City, UT 84112-0111, USA*
[4]*Now at: EOST-Institut de Physique du Globe, 5 rue* René *Descartes, F-67084 Strasbourg Cedex, France*

For Submission: Geophysical Journal International

## SUMMARY

We extended a high-order finite-difference scheme for the elastic *SH* wave equation in axi-symmetric media for use on parallel computers with distributed memory architecture. Moreover we derive an analytical description of the implemented ring source and compare it quantitatively with a double couple source. The restriction to axi-symmetry and the use of high performance computers and PC networks allows computation of synthetic seismograms at dominant periods down to 2.5 seconds for global mantle models. We give a description of our algorithm (SHaxi) and its verification against an analytical solution. As an application, we compute synthetic seismograms for global mantle models with additional stochastic perturbations applied to the background *S*-wave velocity model. We investigate the influence of the perturbations on the *SH* wave field for a suite of models with varying perturbation amplitudes, correlation length scales, and spectral characteristics. The inclusion of stochastic perturbations in the models broadens the pulse width of teleseismic body wave arrivals and delays their peak arrival times. Coda wave energy is also generated which is observed as additional energy after prominent body wave arrivals. The SHaxi method has proven to be a valuable method for

computing global synthetic seismograms at high frequencies and for studying the seismic waveform effects from models where rotational symmetry may be assumed.

## 1 INTRODUCTION

Despite the ongoing increase of computational performance, full 3D global seismic waveform modeling is still a challenge and far from being a routine tool for understanding the Earth's interior. Yet, for teleseismic distances, a substantial part of the seismic energy travels in the great circle plane between source and receiver and can be approximated assuming invariance in the out of plane direction. This motivates algorithms which take advantage of this invariance with a much higher efficiency compared to full 3D methods. A straight forward realization is to ignore the out of plane direction and compute the wave field along the two remaining dimensions. For example, Furumura *et al.* (1998) developed a pseudospectral scheme in cylindrical coordinates and invariance in the direction parallel to the axis of the cylinder for modeling *P*-*SV* wave propagation down to depths of 5000 km. This geometry corresponds to a physical 3D model with the seismic properties invariant along the direction not explicitly modelled. As a consequence, the seismic source is a line source having a substantially different geometrical spreading compared to more realistic point sources.

A different approach which circumvents the line source problem is the axi-symmetric approach. Here the third dimension is omitted as well, but the corresponding physical 3D model is achieved by virtually rotating the 2D domain around a symmetry axis. Seismic sources are placed at or nearby the symmetry axis and act as point sources maintaining the correct geometrical spreading. Since such a scheme can be seen as a mixture between a 2D method (in terms of storage needed for seismic model and wave

field) and a 3D method (since point sources with correct 3D spreading are modeled) such methods are often referred to as 2.5D methods.

A variety of axi-symmetric approaches have been used in the last decades (e.g. Alterman and Karal, 1968). Axi-symmetric wave propagation for SH-waves in spherical coordinates with a FD technique was implemented by Igel & Weber (1995) to calculate seismograms for global Earth models and also by Chaljub & Tarantola (1997) to study frequency dependent effects of *S* and *SS* waves. Furumura and Takenaka (1996) applied a pseudospectral approach to regional applications for distances up to 50 km. Igel & Gudmundsson (1997) also used a FD method to study frequency dependent effects of *S* and *SS* waves. Igel & Weber (1996) developed a FD approach for *P-SV* wave propagation. Thomas *et al.* (2000) developed a multi-domain FD method for acoustic wave propagation and applied the technique to studying precursors to the core phase *PKPdf*. Recently, Toyokuni *et al.* (2005) developed a scheme based on the algorithm of Igel & Weber (1996) with extension to non-symmetric models for modeling a sphere consisting of two connected axi-symmetric half-spheres. Recently, Nissen-Meyer *et al.* (2006) presented a 2D spectral-element method for axi-symmetric geometries and arbitrary double-couple sources.

The main purpose of this paper is to (1) extend the axi-symmetric FD approach of Igel & Weber (1995) for modeling *SH*-wave propagation (SHaxi) for use on parallel computers with distributed memory architecture, (2) examine the properties of the implemented ring source and to show that it can be compared with a double-couple source, (3) as an application, to model the influence of whole mantle scattering on the seismic SH wave field. We furthermore present an application of the SHaxi method to

modeling the *SH*- wavefield in models of whole mantle random *S*-wave velocity perturbations. In a companion paper (Thorne *et al.* 2007) we make an extensive comparison of SHaxi generated seismograms with results from recent data analyses of lower mantle structure. The SHaxi source code is available at: http://www.spice-rtn.org/library/software.

## 2 THE AXI-SYMMETRIC FINITE-DIFFERENCE SCHEME

### 2.1 Formulation of the wave equation

The general 3D velocity stress formulation of the elastic wave equation in spherical coordinates is given by Igel (1999). The coordinate system is shown in Figure 1. The relevant equations for pure SH wave generation are:

$$
\begin{aligned}
\rho \partial_t v_\varphi &= \partial_r \sigma_{r\varphi} + \frac{1}{r}\partial_\theta \sigma_{\theta\varphi} + \frac{1}{r\sin\theta}\partial_\varphi \sigma_{\varphi\varphi} + \frac{1}{r}(3\sigma_{r\varphi} + 2\sigma_{\theta\varphi}\cot\theta) + f_\varphi \\
\partial_t \varepsilon_{r\theta} &= \frac{1}{2}\left(\frac{1}{r}\partial_\theta v_r + \partial_r v_\theta - \frac{1}{r} v_\theta\right) \\
\partial_t \varepsilon_{\theta\varphi} &= \frac{1}{2}\left(\frac{1}{r\sin\theta}\partial_\varphi v_\theta + \frac{1}{r}\partial_\theta v_\varphi - \frac{\cot\theta}{r} v_\varphi\right) \\
\partial_t \varepsilon_{r\varphi} &= \frac{1}{2}\left(\frac{1}{r\sin\theta}\partial_\varphi v_r + \partial_r v_\varphi - \frac{1}{r} v_\varphi\right),
\end{aligned}
\tag{1}
$$

with: $\sigma_{ij}$: Stress tensor, $v_\varphi$: $\varphi$-component of velocity, $f_\varphi$: external force, $\varepsilon_{ij}$: Strain tensor, and $\rho$: density.

In the axi-symmetric system, Eq. 1 can be further simplified by assuming the external source and model parameters are invariant in the $\varphi$-direction. The resultant equations are:

$$
\rho \partial_t v_\varphi = \partial_r \sigma_{r\varphi} + \frac{1}{r}\partial_\theta \sigma_{\theta\varphi} + \frac{1}{r}(3\sigma_{r\varphi} + 2\sigma_{\theta\varphi}\cot\theta) + f_\varphi
$$

$$\partial_t \varepsilon_{\theta\varphi} = \frac{1}{2}\left(\frac{1}{r}\partial_\theta v_\varphi - \frac{\cot\theta}{r} v_\varphi\right) \qquad (2)$$

$$\partial_t \varepsilon_{r\varphi} = \frac{1}{2}\left(\partial_r v_\varphi - \frac{1}{r} v_\varphi\right)$$

Due to axi-symmetry, spatial properties vary solely in the $r$ and $\theta$-directions. Hence the computational costs of this formulation are comparable to 2D methods, while the correct 3D spreading of the wave field is still preserved, in contrast to purely 2D methods, provided the source is centred at the symmetry axis. Due to the cot($\theta$) term in Eq. 2, *SH* motion is undefined directly on the symmetry axis and the seismic source can not be placed there. We discuss the seismic source below.

A staggered grid scheme was used for the discretization of the seismic parameters, so the stress components and the velocity are calculated at different locations. A schematic representation of the grid is shown in Figure 2. In addition to the grid points which define the model space, auxiliary points were added above the Earth's surface, below the core-mantle boundary (CMB) and beyond the symmetry axis ($\theta < 0°$ and $\theta > 180°$) for the calculation of the boundary conditions (discussed below).

**2.2 The properties of the *SH* ring source**

Due to axi-symmetry it is not possible to implement sources which generate the *SH* portion of an arbitrary oriented double couple. Moreover, exact point sources are not possible since *SH* motion is not defined directly at the axis but can be approximated when the wavelength of interest is made sufficiently larger than the grid size. We will discuss the properties of the implemented axi-symmetric *SH* source and show that its displacement far-field is proportional to that of an appropriately oriented double-couple source.

**Ring source expression**

The SH ring source corresponds to the one used by Chaljub & Tarantola (1997) which found that the relative amplitude of the source depends on the take-off angle γ as sin(γ). However, the complete source solution was not given although this is essential to perform a quantitative comparison of numerical and analytical solution. In order to derive the analytical solution of an SH ring source of infinitesimal size in a homogeneous isotropic elastic media, it is convenient to use Eq. (4.29) of Aki & Richards (2002), which gives the displacement field due to couples of forces, each of moment $M_{pq}$. We start by noting that the ring source can be seen as the summation of individual couples of forces $F$ over half the perimeter of a circle (see Figure 3), keeping in mind that the radius $R$ ultimately tends to 0 and the forces tend to $+\infty$, so as to have a finite moment (this is analogous to the discussion p. 76 of Aki & Richards (2002)).

Projecting the forces on the axes $x_1$ and $x_2$, we can write that the moment due to this couple is

$$dM(\psi) = 2F\cos(\psi)\cdot R\cos(\psi) - 2F\sin(\psi)\cdot R\sin(\psi) \tag{3}$$

with $F = \left|\vec{F}\right|$, and $\Psi$ the orientation of the individual couple of forces $F$ (see Fig. 3).

Obviously, the total moment $M_0$ due to the ring force is $M_0 = 2\pi FR$, so the contributions from $M_{21}$ and $M_{12}$ are $(M_0/\pi)\cdot\cos^2(\Psi)$ and $-(M0/\pi)\cdot\sin^2(\Psi)$, respectively. Inserting those expressions in Eq. (4.29) of Aki and Richards (2002), and further integrating from 0 to $\pi$, provides the full displacement field of an SH ring source of infinitesimal size:

$$v_\varphi^{Ring}(s,\gamma,t) = \sin(\gamma)\frac{-\beta M_0(t-s/\beta) + s\dot{M}_0(t-s/\beta)}{8\pi\rho\beta^3 s^2}, \tag{4}$$

with: $v_\varphi^{Ring}$ : $\varphi$-component of displacement, $\rho$: density, $\beta$: $S$-wave velocity, $M_0(t)$, $\dot{M}_0(t)$: seismic moment and moment rate, $t$: $S$-wave travel time, $s$: source-receiver distance, and

$\gamma$: take-off angle (see Fig. 1). This source will be compared with the far-field term of a strike-slip source (in the $x_1/x_3$ plane with slip along $x_1$) in the nodal plane for *P* radiation ($\varphi$=0). Using the equations analogous to Eq. 4.32 and 4.33 of Aki & Richards (2002) (with appropriate permutation of axis) we get:

$$v^{DC}(s,\gamma,t) = \sin(\gamma)\frac{\dot{M}_0(t-s/\beta)}{4\pi\rho\beta^3 s}. \quad (5)$$

We see that the far-field terms in Eq. 4 and Eq. 5 only differ by a factor 2. Hence, in the nodal plane for *P* radiation and for distances where the near and intermediate term can be neglected (i.e. more than a few dominant wavelengths, which is fulfilled for teleseismic investigations), the wave field of the SH ring source of infinitesimal size can be compared to that of the corresponding strike-slip source.

In contrast to the infinitesimal SH ring source described by Eq. 4, the source implemented in SHaxi is a finite ring. Yet, as we show in Section 3, the similarity between seismograms calculated for either source is close enough that the approximation of an infinitesimal ring source can be made.

**2.3 Boundary conditions**

At the symmetry axis, the free surface, and the CMB, adequate boundary conditions must be applied. For the horizontal surfaces (the CMB can be treated similarly to the free surface since *SH* waves reflect totally at both boundaries) the boundary condition is given by the zero-stress condition which requires $\sigma_{r\varphi} = 0$ for the surface (e.g., Levander 1988; Graves 1996). Due to the staggered grid scheme $\sigma_{r\varphi}$ is not defined exactly on the free surface but a half grid spacing below the surface (Figure 2). Therefore the zero-stress condition is realized by giving the auxiliary $\sigma_{r\varphi}$ grid points above the surface the inverse values of their counterparts below the surface at each time step

(Figure 4). This results in a vanishing stress component at the surface in a first order sense. For the symmetry axis, the boundary conditions are derived from geometric constraints: all grid points beyond the axis are set to the values of their partners inside the model space, meaning that the fields are extended according to the axi-symmetry condition. Directly at the axis $v_\varphi$ and $\sigma_{r\varphi}$ are set to zero since both values are undefined here according to Eq. 2. In general, the number of rows of auxiliary grid points which have to be added correspond to half the length of the FD operator used for the boundary condition. This enables the FD operator to operate across the boundary and calculate a derivative for grid points residing directly at the boundary. For the simulations shown here a FD operator length of 2 at the model boundaries corresponding to one row of extra grid points is added. For the boundary at the symmetry axis this choice is crucial because convergence to the analytical solution is achieved *only* for the two-point FD operator. We do not yet understand why higher order operators fail here. For the grid points off of the boundaries a 4-point FD operator is used.

**2.4 Parallelization**

Actual high performance computers or workstation clusters usually consist of several units of processors (nodes) each having their own private memory. These nodes work independently and are interconnected for synchronization and data exchange. In order to take advantage of such systems the model space is divided horizontally in several *domains*. Each domain can now be autonomously processed by a single node. Figure 5 shows such a *domain decomposition* for a total number of three domains. Similarly to the implementation of the boundary conditions described above, auxiliary grid points are added adjacent to the domain boundaries for the communication between the nodes. This

communication is implemented using the Message Passing Interface (MPI) library. The values of these auxiliary points are updated at each time step from their counterparts in the adjacent domain as indicated by the arrows in Figure 5 (points with identical column indices – underlain in gray). The number of columns of the auxiliary points must be equal to half of the FD operator length. We use a 4-point FD operator inside the model; therefore the auxiliary regions must be 2 points wide.

**2.5 Computational costs**

Compared to 3D modeling techniques the resources necessary for SHaxi simulations are comparatively low. Simulations with relatively long periods ~10-20 seconds can be done on a single PC within a couple of hours. For shorter periods the required memory and processing time increases strongly: The highest achievable dominant frequency $f_{DOM}$ of the seismograms is inversely proportional to the grid spacing $dx$, whereas the time increment between two iterations is proportional to $dx$. Thus the memory needed to store the (2D) grids is proportional to $f_{DOM}^2$ and the time needed to perform a simulation is proportional to $f_{DOM}^3$. A further performance increase can be achieved by limiting the model space in $\theta$-direction by the maximum epicentral distance of interest. This reduces the number of grid points and consequently the needed memory and simulation time. The requirements on the system used for the simulations in this study give an idea about the achievable frequencies on supercomputers and PC clusters: The 24-node, 2.4 GHz PC-cluster located at Arizona State University is capable of computing dominant periods down to 6 s for *S* waves at 80° distance (Table 1). For a simulation time of 2700s the run time was about 2 ¼ days and each node needed 428 Mb of memory. The 5 TFlop/s system of the Arctic Region Supercomputing Center “Iceberg"

needed for the same run about 15.5 hours (Table 2). In general, on current supercomputer systems with peak performances well beyond 1 TFlop/s dominant periods below 1s can be achieved.

## 3 COMPARISON WITH THE ANALYTICAL SOLUTION

A first comparison of axi-symmetric FD methods was done by Igel *et al.* (2000). Good waveform fits of single seismograms were achieved for body waves, although the *SH* source was not examined in detail. In order to show that the SHaxi method provides the correct wave field we compare synthetic seismograms for two receiver setups with the analytical solution of a ring source (Eq. 4) in an infinite homogeneous media, with parameters shown in Table 3. The size of the numerical model was chosen so that reflected waves from the model boundaries were significantly delayed and therefore not interfering with the time window of interest. To quantify the difference between synthetic seismograms computed using SHaxi with the analytic solution, the energy misfit of the seismograms was computed. The energy misfit $E$ of a time series $x_i$ with respect to a reference series $y_i$ is given by:

$$E = \frac{\sum (x_i - y_i)^2}{\sum y_i^2}, \tag{8}$$

(e.g., Igel *et al.* 2001). Good agreement between the seismograms and the analytic solution can be said to be attained if the energy misfit is below 1%. Two receiver configurations, shown in Figure 6a and 7a, were used for the following purposes: (1) a circular array consisting of 15 evenly spaced receivers placed on a half circle with the source in its center. This setup covers the whole range of possible take off angles and is optimally suited for investigating the angular source radiation; (2) a linear array with the receivers placed on a straight horizontal line originating from the source. With this linear

array the propagation effects and the spreading for a constant take off angle and varying source receiver distance can be investigated. Table 3 lists the simulation parameters for the two setups. Figure 6 shows the results for the circular array. In Figure 6b the computed seismograms (red) together with the analytical traces (black) are displayed. To make the difference between both solutions apparent, the topmost trace shows the difference trace for receiver no. 8 scaled by a factor of 25. Figure 6c shows the radiation pattern for all computed traces (marked with red circles) together with the analytical curve $f(\gamma) = \sin(\gamma)$, with $\gamma$ the take off angle, plotted with solid lines. The SHaxi radiation pattern is calculated from the maximum amplitudes of the individual seismogram traces.

Figure 6d shows the energy misfit between the SHaxi solution and Eq. 4. The energy misfit is well below 0.4% and depends on the take off angle. For steep angles the accuracy of the solution decreases. This behavior is caused by the boundary condition for the symmetry axis which works best for take off angles perpendicular to the axis.

In Figure 7b the numerical (red) and analytical (black) seismograms for the linear array are shown. In Fig. 7c the geometrical spreading of both solutions are shown similar to Fig. 6c. The analytical function is $f(r) \sim 1/r$ with $r$: source-receiver distance. The bottom right figure shows the energy misfit for the linear array. Except for receiver 1 the energy misfit is below 0.4%. The increased energy misfit for locations very close to the source is a numerical effect caused by the grid discretization. This effect occurs for source-receiver distances closer than one dominant wavelength which should be avoided to achieve an acceptable misfit.

In summary, the method is capable of computing the far field portion of a strike-slip source in the nodal plane for *P* radiation. Thus, for teleseismic investigations where

the wave field travels many dominant wavelengths to the receiver SHaxi provides correct seismograms. In the next Section we will show an SHaxi application which illustrates the potential of this method.

## 4 APPLICATION: SCATTERING FROM THE WHOLE MANTLE

Propagating seismic waves lose energy due to geometrical spreading, intrinsic attenuation and scattering attenuation. The scattering, or interaction with small spatial variations of material properties, of seismic waves affects all seismic observables including amplitudes and travel-times and also gives rise to seismic coda waves. In order to demonstrate the usability of the SHaxi method at high frequencies we present a comparison of synthetics computed from purely elastic models that have been stochastically perturbed from the PREM reference model (Dziewonski & Anderson, 1981).

A central question for the interpretation of such axi-symmetric scattering models is how parameters such as perturbation amplitude and correlation length of the axi-symmetric model can be transferred to the corresponding 3D perturbations of the Earth's mantle. Unfortunately, no numerical comparison of 3D versus axi-symmetric scattering models has been performed yet. Such a study would require extremely high computational resources in order to generate synthetics for full 3D geometries at the dominant periods of interest and is beyond the scope of this paper. Nevertheless, the insights would be highly valuable, e.g. for the calibration of other scattering simulation methods. A candidate method for such a study is the spectral-element method (Komatitsch & Tromp, 1999). Stochastical approaches like the multi-phonon method (Shearer & Earle, 2004) may provide a more realistically obtainable comparison. Alternatively, we discuss here the

expected influence of axi-symmety on the seismic wavefield from plausibility considerations and by comparison with comparable studies:

For models with no variations perpendicular to the great circle plane, axi-symmetric and 3D modeling provide the same results. However, for the Earth's mantle a locally varying, arbitrary oriented structure is plausible which is impossible to parameterize using an axi-symmetric system. Instead, axi-symmetric stochastical models are invariant in out-of-plane direction, resulting in model variations which are actually ring shaped with the center at the symmetry axis.

This geometry causes two significant competing effects on the coda of the seismograms: (1) scattered energy can not get lost by radiation off the great circle plane which leads to an enhanced contribution to the scattering amplitudes. In opposition to this effect, (2) in 3D random media the initial wavefront will encounter more possible scatterers than in 2D and thus contributions from off-plane scattering to the seismogram coda are missing in the axi-symmetric case, which causes a reduction of the scattering amplitudes. It is unclear which of these two effects is dominant and the authors are unaware of any studies that have quantified the two effects for 2D v. 3D geometries on the shape and characteristics of the coda wavetrain.

For a precise understanding of these effects the aforementioned 3D calculations have to be performed. However, results from Frenje & Juhlin (2000) provide indications that the influence on the scattering coda is negligible. Frenje & Juhlin compared Cartesian 2D and 3D finite-difference simulations with single scattering theory. They found no significant differences between 2D and 3D simulations when measuring scattering

attenuation, except that 2D simulations provide less stable results of the derived parameters.

This increased instability of 2D simulations is caused by the stronger influence of the specific model realization for a given set of model parameters: The off-plane model variations in the 3D case average out the effects of the specific model realization on the scattering coda, whose properties depend mainly on perturbation amplitude and correlation length. For 2D simulations this averaging process does not exist. However, stable model parameters can be derived by analyzing multiple realizations of a set of model parameters.

**4.1 Inference of whole mantle scattering**

Many techniques have been developed to study the properties of seismic scattering (see Sato & Fehler, 1998 for a discussion on available techniques). Advances in computational speed have allowed numerical methods such as FD techniques to be used in analyzing seismic scattering (e.g., Frankel & Clayton 1984, 1986; Frankel 1989; Wagner 1996). The majority of FD studies had thus far focused on *S*-wave scattering in regional settings with source-receiver distances of just a few hundred kilometers. Thus, these recent advances have greatly improved our understanding of scattering in the lithosphere where strong scattering is apparent with $V_S$ perturbations on the order of 5 km in length and 5% RMS velocity fluctuations (e.g., Saito *et al.* 2003).

Recently, small-scale scattering has been observed near the core-mantle boundary (CMB). Cleary & Haddon (1972) first recognized that precursors to the *PKP* phase may be due to small scale heterogeneity near the CMB. Hedlin *et al.* (1997) also modeled *PKP* precursors, with a global data set. They concluded that the precursors are best

explained by small-scale heterogeneity throughout the mantle instead of just near the CMB. Hedlin *et al.*'s (1997) finding suggests scatterers exist throughout the mantle with correlation length scales of roughly 8 km and 1% RMS velocity perturbation. Margerin & Nolet (2003) also modeled *PKP* precursors corroborating the Hedlin *et al.* (1997) study that whole mantle scattering best explains the precursors, although Margerin & Nolet suggest a slightly smaller RMS perturbations of 0.5% on length scales from 4 to 24 km. Lee & Sato (2003) examined scattering from *S* and *ScS* waves beneath central Asia, finding that scattering from *ScS* waves may dominate over the scattering from *S* waves at dominant periods greater than 10s and that as much as 80% of the total attenuation of the lower mantle may be due to scattering attenuation. Because Lee & Sato (2003) used radiative transfer theory to model the scattering coefficient, it is not possible to directly translate the scattering coefficients determined in their study to correlation length scales or RMS perturbations (personal communication, Haruo Sato, 2005) for comparison with the studies of Hedlin *et al.* (1997) or Margerin & Nolet (2003). Nevertheless, their conclusion is important in that whole mantle scattering is necessary to model their data.

Baig & Dahlen (2004) sought to constrain the maximum allowable RMS heterogeneity in the mantle as a function of scale length. Their study also suggests that as much as 3% RMS *S*-wave velocity perturbations are possible for the entire mantle for scale lengths less than about 50 km. Baig & Dahlen (2004) also suggest that in the upper 940 km of the mantle, scattering may be twice as strong as in the lower mantle. The suggestion of stronger upper mantle scattering is also supported by Shearer & Earle (2004). They find that, in the lower mantle, 8 km scale length heterogeneity with 0.5% RMS perturbations can explain *P* and *PP* coda for earthquakes deeper than 200 km. They

also find that shallower earthquakes require stronger upper mantle scattering with 4-km scale lengths and 3-4% RMS perturbations.

Although a growing body of evidence suggests that whole mantle scattering is necessary to explain many disparate seismic observations, the characteristic scale lengths and RMS perturbations are determined using analytical and semi-analytical techniques which in many cases are based on single-point scattering approximations and do not synthesize waveforms. As whole mantle scattering may affect all aspects of seismic waveforms, it is thus important to synthesize global waveforms with the inclusion of scattering effects. The first attempt at synthesizing global waveforms was by Cormier (2000). He used a 2-D Cartesian pseudo-spectral technique to demonstrate that the D" discontinuity may be due to an increase in the heterogeneity spectrum. Cormier (2000) suggests that as much as 3% RMS perturbations may be possible for length scales down to about 6 km.

In this study we generate a suite of random models of different statistical properties based on PREM. Seismograms of these models are compared and discussed. Moreover the potential and the restrictions of the SHaxi method concerning investigations on whole mantle scattering are discussed.

**4.2 Implementation of random velocity perturbations in SHaxi**

Models of random velocity perturbations (referred to as random media hereafter) are characterized by their spatial autocorrelation function (ACF), the Fourier transform of which equals the power spectrum of the velocity perturbations. Construction of random media for FD simulations is implemented using a Fourier based method (e.g., Frankel &

Clayton 1986; Ikelle *et al.* 1993; Sato & Fehler 1998) which can be written as a convolution:

$$M(x_i, y_k) = R(x_i, y_k) * ACF(x_i, y_k), \tag{9}$$

With $x_i,y_k$: coordinates of a Cartesian grid, $R(x_i,y_k)$: random matrix, $ACF(x_i,y_k)$: autocorrelation function, $M(x_i,y_k)$: the resulting model perturbation, and *: the convolution operator. For performance issues the convolution is replaced by multiplication in the Fourier space using the 2D Fast Fourier Transform $\Im$ and its inverse $\Im^{-1}$:

$$M(x_i, y_k) = \Im^{-1}(\Im(R(x_i, y_k)) \cdot \Im(ACF(x_i, y_k))) \tag{10}$$

The most popular choices of ACFs are defined in Frankel & Clayton (1986) as:

· Gaussian: $$ACF(x,y) = e^{-r^2/a^2}, \tag{11}$$

· Exponential: $$ACF(x,y) = e^{-r/a}, \tag{12}$$

· von Kármán: $$ACF(x,y) = \frac{1}{2^{m-1}\Gamma(m)}\left(\frac{r}{a}\right)^m K_m\left(\frac{r}{a}\right), \tag{13}$$

where $r$ is the offset or spatial lag: $r = \sqrt{x^2 + y^2}$, $a$ is the autocorrelation length (ACL), $K_m(x)$ is a modified Bessel function of the second kind of order $m$ and $\Gamma(m)$ is the gamma function. The power spectrum of an ACF is flat out to a corner wavenumber that is roughly proportional to the inverse of the ACL. From the corner wavenumber the power spectrum asymptotically decays. The primary difference between ACFs is their roughness, which is defined as how fast the rate of fall off is in the decaying portion of the power spectrum. The most important factor that the roughness of the ACF affects is the frequency dependence of scattering (e.g., Wu 1982). We construct models of random

media using the ACFs defined in Eqs. 11-13, noting that other choices of ACFs also exist (e.g., Klimeš 2002a; 2002b).

Challenges arise in implementing random media in SHaxi as the Fourier technique (e.g., Frankel & Clayton 1986) is defined on a Cartesian grid and not on the spherical grid used in SHaxi. Using this Cartesian grid $M(x_i,y_k)$ directly as spherical grid in SHaxi would therefore lead to an artificial anisotropy due to the now decreasing grid spacing for increasing depth. To avoid this, $M(x_i,y_k)$ is first calculated on a very fine Cartesian grid which contains the SHaxi model space. Then the $V_S$ perturbations at the SHaxi grid points $M(\theta_i,r_k)$ are interpolated from $M(x_i,y_k)$ using a near neighbor algorithm. The $V_S$ perturbations are then applied to the PREM background model. $V_S$ perturbations are clipped at ±3 times the RMS $V_S$ perturbation in order to avoid extreme perturbations that may affect the finite difference simulations. Analysis of the statistical properties of the original Cartesian random media $M(x_i,y_k)$ and the interpolated random media $M(\theta_i,r_k)$ on SHaxi's grid show no significant difference. However, the creation of the very large initial Cartesian grid and the interpolation to the SHaxi grid points makes this method of model generation unhandy. A promising approach for a direct model generation using the Karhunen-Loève Transform was recently developed by Thorne *et al.* (2008). Figure 8 shows an example of random media interpolated onto SHaxi's grid.

Fully 3D random media cannot be incorporated in SHaxi because of the axi-symmetric approximation. As explained in Section 1.1 model invariance in the $\varphi$-direction causes the random perturbations to effectively be zero in this direction. The effect of this apparent anisotropic ACF in SHaxi will likely be to produce less scattering than for fully 3D models (e.g., Makinde *et al.* 2005). We compute synthetic seismograms

for a suite of realizations of random media with ACLs of 8, 16, and 32 km and RMS $V_S$ perturbations of 1, 3, and 5%. The ACL range corresponds to the scattering regime of SH waves, which typically have dominant periods in the order of 4s and an average dominant wavelength of 24 km for the chosen geometry. We analyze the effect of these random $V_S$ perturbations on *S* and *ScS* waveforms in the distance range 65° to 75° for a source depth of 200 km.

**4.3 Whole mantle scattering simulation results**

The effect of random media on the seismic wave field is shown in Fig. 9. The left part displays the seismic wave field at one snapshot in time (300s) for a 200-km-deep event for the unperturbed PREM reference model. The wave fronts for the seismic phases *S* and *sS* are labeled. Smaller amplitude arrivals are also apparent, corresponding to reflections from the transition zone and upper mantle discontinuities in the PREM model. The right part shows the effect on the wave field for the same snapshot in time, when the PREM model has random $V_S$ variations applied. Significant coda wave development is observed in the wave field. Furthermore, the smaller amplitude arrivals that were clearly visible in the upper panel are barely discernible within the scattered wave field.

The frequency dependence of scattering is displayed in Figure 10. Here synthetics computed for an epicentral distance of 75° are shown for a Gaussian ACF with 3% RMS perturbations and ACL of 16 km overlain on top of synthetics computed for the PREM model. The effects of scattering are most pronounced for the shortest dominant period synthetics. Here the direct *S*-arrival is broadened with a delay of the peak energy of roughly two seconds. A similar effect is observed for the *ScS* arrival. Substantial energy is also seen between the *S* and *ScS* arrivals that do not appear in the PREM synthetics.

However, for longer period waveforms, these scattering effects become less apparent, and for dominant periods of 20s, the PREM and Gaussian ACF synthetics are nearly identical. This is due to the short-scale length of the random perturbations applied to the model. As the dominant wavelength of the propagating energy increases to values significantly greater than the dominant wavelength of the random media the propagating energy can much easier heal around the perturbations.

The effect of ACL on the waveform shape is demonstrated in Figure 11 for models produced with Gaussian ACF's. The largest amount of scattering is observed for the largest ACL of 32 km. Here the absolute amplitude of the *S* arrival is most significantly reduced as more energy is robbed from the direct *S*-wave to go into later arrivals. Significant delay in *S*-wave peak arrival time is also apparent which may strongly affect the results of cross-correlation techniques at picking arrival times.

Note that there is potentially non-uniqueness in determining scattering structure. For many observable properties of the wave field, such as delay time of peak arrivals, broadening of the arrivals wave packets, and coda energy, it may be very difficult to distinguish between various models. E.g., A Gaussian ACF with ACL=8 km and RMS=3% behaves very similarly to an Exponential ACF with ACL=32 km and RMS=1%. Ultimately distinguishing between these various models will require examination of data in a range of frequencies.

**4.4 Discussion of the scattering simulation results**

Scattering in the mantle affects all parts of the seismic waveform and may account for a significant portion of the total attenuation we map into the lower mantle. We have implemented scattering in a global numerical method, but much work needs to

be done in comparing our results with data and in producing more realistic models of mantle scattering. For example, models with anisotropic ACF's in the lateral direction or models with differing ACL's or ACF's in different layers of the mantle may provide better approximations to the Earth structure.

Yet, it is difficult to implement multi-layered models using the Fourier technique to produce random velocity perturbations. Different models have to be constructed on Cartesian grids and then interpolated onto the SHaxi grid. This will produce undesirable first-order discontinuities in between layers with different scattering properties.

SHaxi is a viable technique for which models of whole mantle scattering can be implemented. Although fully 3D techniques exist, it is still impossible to model scattering in 3D because current computational limits do not allow for computation of the wave field at the small dominant periods where scattering effects are observed in the Earth. Furthermore, the SHaxi method may provide a better alternative to finite frequency approximations of scattering since the entire wave field is computed and there is no reliance on single-point scattering approximations. Our results are calculated for elastic velocity models and do not include intrinsic attenuation. Inclusion of inelasticity may weaken the effects of multiple scattering (e.g., Yomogida & Benites, 1996), yet future efforts should combine both attenuation mechanisms.

## 5 DISCUSSION AND CONCLUSIONS

In this paper, we presented a method to calculate high-frequency global *SH* seismograms for axi-symmetric geometries. Axi-symmetric methods fill the gap between 1D methods which are often too limited to explain teleseismic observations and full 3D methods, which require very high computational resources. On teleseismic scales the major portion

of the wave field propagates in the great circle plane. As a consequence, out of plane variations of the seismic properties can often be ignored. Although the computational effort of SHaxi is equivalent to 2D methods the correct 3D geometrical spreading is preserved in contrast to traditional 2D methods. The applied ring-source in SHaxi is equivalent to a vertical strike-slip source for source-receiver distances larger than about five dominant wavelengths where the near and intermediate wave fields vanish. Although arbitrary sources cannot be modeled and comparisons with real seismograms can not be directly made, the method can be used to probe many teleseismic questions. The method is especially suited to investigating relative amplitudes and/or travel-times. Moreover when the take-off angle of the investigated phases is known, amplitude correction terms can be calculated. The reduction of computational effort has permitted exploration of teleseismic waveforms at frequencies where whole mantle scattering may come into play. For example, determination of the length scales and spatial location of small scale seismic heterogeneity may provide important geodynamic implications, such as the degree of convective mixing in the mantle or compositional heterogeneity (e.g., van der Hilst & Kárason 1999; Davies 2002). Fixing the spatial extent of small scale heterogeneity in the mantle may be challenging, however techniques focused on measuring differential attenuation may prove useful. A companion paper (Thorne *et al.* 2007) uses SHaxi to examine the high frequency wave form effects of recent data analyses for D" discontinuity structure beneath the Cocos Plate region. As investigations of whole mantle scattering become more and more prominent, numerical techniques such as SHaxi that are capable of synthesizing waveforms with the inclusion of scattering will become important, as they have for regional scale modeling.

**Acknowledgements**

G. Jahnke was supported by the German Research Foundation (DFG, Project Ig16/2). M. Thorne was partially supported by NSF grant EAR-0135119 and the International Quality Network: Georisk funded by the German Academic Exchange Service. We thank the Arctic Region Supercomputing Center of the University of Alaska Fairbanks and the Leibniz Rechenzentrum Munich for access to their computational facilities. We also acknowledge support from the European Human Ressources Mobility Program (SPICE Project) for travel support and for hosting the SHaxi code (www.spice-rtn.org). Finally, we thank two anonymous reviewers, E. Saenger, and editor J. Virieux for their constructive comments which helped to improve the paper.

**References**

Aki, K. & Richards, P. G., 2002. Quantitative seismology, 2nd Edition, *University Science Books.*

Alterman, Z., & Karal, F. C., 1968. Propagation of elastic waves in layered media by finite-difference methods, *Bull. Seism. Soc. Am.*, **58**, 367-398.

Baig, A.M., & Dahlen, F.A., 2004. Traveltime biases in random media and the *S*-wave discrepancy, *Geophysical Journal International*, **158**, 922-938.

Chaljub, E. & Tarantola, A., 1997. Sensitivity of *SS* precursors to topography on the upper-mantle 660-km discontinuity. *Geophys. Res. Lett.*, **24** (21), 2613-2616.

Cleary, J.R., & Haddon, R.A.W., 1972. Seismic wave scattering near core-mantle boundary – new interpretation of precursors to PKP, *Nature*, **240** (5383), 549.

Cormier, V.F., 2000. D" as a transition in the heterogeneity spectrum of the lowermost mantle. *J. Geophys. Res.*, **105**, 16193-16205.

Davies, G.F., 2002. Stirring geochemistry in mantle convection models with stiff plates and slabs. *Geochemica et Cosmochimica Acta*, **66** (17), 3125-3142.

Dziewonski, A. M. & Anderson, D.L., 1981. Preliminary reference Earth model, *Phys. Earth Planet. Inter.,*, **25**, 297-356.

Frankel, A., & Clayton, R.W., 1984. A Finite Difference Simulation of Wave Propagation in Two-dimensional Random Media, *Bull. Seism. Soc. Am.*, **74** (6), 2167-2186.

Frankel, A., & Clayton, R.W., 1986. Finite Difference Simulations of Seismic Scattering: Implications for the Propagation of Short-Period Seismic Waves in the Crust and Models of Crustal Heterogeneity, *J. Geophys. Res.*, **91** (B6), 6465-6489.

Frankel, A., 1989. A Review of Numerical Experiments on Seismic Wave Scattering, *Pure and Applied Geophysics*, **131** (4), 639-685.

Frenje, L., Juhlin, C., 2000. Scattering attenuation: 2-D and 3-D finite difference simulations vs. theory, *Journal of Applied Geophysics*, **44**, 33-46.

Furumura, T., Kennett, B.L.N., & Furumura, M., 1998. Seismic wavefield calculation for laterally heterogeneous spherical earth models using the pseudospectral method, *Geophys. J. Int.,* **135**, 845-860.

Furumura T. & Takenaka, H., 1996. 2.5-D modeling of elastic waves using the pseudospectral method, *Geophys. J. Int.*, **124**, 820-832.

Graves, R.W., 1996. Simulating seismic wave propagation in 3D elastic media using staggered-grid finite differences, *Bull. Seism. Soc. Am.*, **86** (4), 1091-1106.

Hedlin, M.A.H, Shearer, P.M., & Earle, P.S., 1997. Seismic evidence for small-scale heterogeneity throughout Earth's mantle, *Nature*, **387**, 145.

Igel, H., 1999. Wave propagation in three-dimensional spherical sections by the Chebyshev spectral method, *Geophys. J. Int.,* **136**, 559-566.

Igel, H., & Gudmundsson, O. 1997., Frequency-dependent effects on travel times and waveforms of long-period S and SS waves, *Phys. Earth Planet. Inter.,* **104**, 229-246.

Igel, H., Nissen-Meyer, T., & Jahnke, G., 2001. Wave propagation in 3-D spherical sections: effects of subduction zones, *Phys. Earth Planet. Inter.,* **132**, 219-234.

Igel, H., Takeuchi, N., Geller, R. J., Megnin, C., Bunge, H. P., Clevede, E., Dalkolmo, J. & Romanowicz, B., 2000. The COSY Project: verification of global seismic modeling algorithms, *Phys. Earth Planet. Inter.,* **119**, 3-23.

Igel, H., & Weber, M., 1995. SH-wave propagation in the whole mantle using high-order finite differences, *Geophys. Res. Lett.,* **22** (6), 731-734.

Igel, H., & Weber, M., 1996. P-SV wave propagation in the Earth's mantle using finite-differences: application to heterogeneous lowermost mantle structure, *Geophys. Res. Lett.*, **23**, 415-418.

Ikelle, L.T., Yung, S.K., & Daube, F., 1993. 2-D random media with ellipsoidal autocorrelation functions, *Geophysics*, **58** (9), 1359-1372.

Klimeš, L., 2002a. Correlation Functions of random media, *Pure and Applied Geophysics,* **159**, 1811-1831.

Klimeš, L., 2002b. Estimating the correlation function of a self-affine random medium, *Pure and Applied Geophysics*, **159**, 1833-1853.

Komatitsch, D. & Tromp, J., 1999. Introduction to the spectral-element method for 3-D seismic wave propagation, *Geophys. J. Int.*, **139**, 806-822.

Lee, W., & Sato, H., 2003. Estimation of S-wave scattering coefficient in the mantle from envelope characteristics before and after the ScS arrival, *Geophys. Res. Lett.,* **30** (24), 2248.

Levander, A.R., 1988. Fourth-order finite-difference P-SV seismograms. *Geophysics*, **53** (11), 1425-1436.

Makinde, W., Favretto-Cristini, N., & de Bazelaire, E., 2005. Numerical modeling of interface scattering of seismic wavefield from a random rough interface in an acoustic medium: comparison between 2D and 3D cases, *Geophysical Prospecting*, **53**, 373-397.

Margerin, L., & Nolet, G., 2003. Multiple scattering of high-frequency seismic waves in the deep Earth: Modeling and numerical examples, *J. Geophys. Res.,* **108** (B5), doi:10.1029/2002JB001974.

Nissen-Meyer, T., Fournier, A., & Dahlen, F. A., 2006. A 2-D spectral-element method for computing spherical-earth seismograms - I. Moment-tensor source, *Geophys. J. Int.*, in press.

Saito, T., Sato, H., Fehler, M., & Ohtake, M. 2003. Simulating the envelope of scalar waves in 2D random media having power-law spectra of velocity fluctuation, *Bull. Seism. Soc. Am.*, **93** (1), 240-252.

Sato, H., & Fehler, M.C., 1998. Seismic Wave Propagation and Scattering in the Heterogeneous Earth, *Springer-Verlag*, New York, 308 pages.

Shearer, P.M., & Earle, P.S., 2004. The global short-period wavefield modeled with a Monte Carlo seismic phonon method. *Geophys. J. Int.*, **158**, 1103-1117.

Thomas, C., Igel, H., Weber, M., & Scherbaum, F., 2000. Acoustic simulation of P-wave propagation in a heterogeneous spherical Earth: Numerical method and application to precursor energy to PKPdf, *Geophys. J. Int.* **141**, 307-320.

Thorne, M.S., Lay, T., Garnero, E.J., Jahnke, G., & Igel, H., 2007. Seismic imaging of the laterally varying D" region beneath the Cocos Plate, *Geophys. J. Int.*, **170**, 635-648, doi: 10.1111/j.1365-246X.2006.03279.x.

Thorne, M.S., Meyers, S.C., Harris, D.B., Rodgers, A.J., 2006. Finite difference simulation of seismic scattering in random media generated with the Karhunen-Loève Transform, *Bull. Seism. Soc. Am.*, in prep.

Toyokuni, G., H. Takenaka, Y. Wang, & B.L.N. Kennett, 2005. Quasi-spherical approach for seismic wave modeling in a 2-D slice of a global earth model with lateral heterogeneity, *Geophys. Res. Lett.,* **32**.

van der Hilst, R.D. & Kárason, H., 1999. Compositional Heterogeneity in the Bottom 1000 Kilometers of Earth's Mantle: Toward a Hybrid Convection Model, *Science*, **283**, 1885-1888.

Virieux, J., 1984, SH-wave propagation in heterogeneous media: Velocity-stress finite-difference method, *Geophysics.,* **49**, 1933-1942.

Wagner, G.S., 1996. Numerical Simulations of Wave Propagation in Heterogeneous Wave Guides with Implications for Regional Wave Propagation and the Nature of Lithospheric Heterogeneity, *Bull. Seism. Soc. Am.*, **86** (4), 1200-1206.

Wu, R.-S., 1982. Attenuation of Short-period Seismic Waves due to Scattering, *Geophys. Res. Lett.*, **9**, 9-12.

Yomogida, K., & Benites, R. 1996. Coda Q as a Combination of Scattering and Intrinsic Attenuation: Numerical Simulations with the Boundary Integral Method, *Pure and Applied Geophysics,* **148**, 255-268.

**FIGURES**

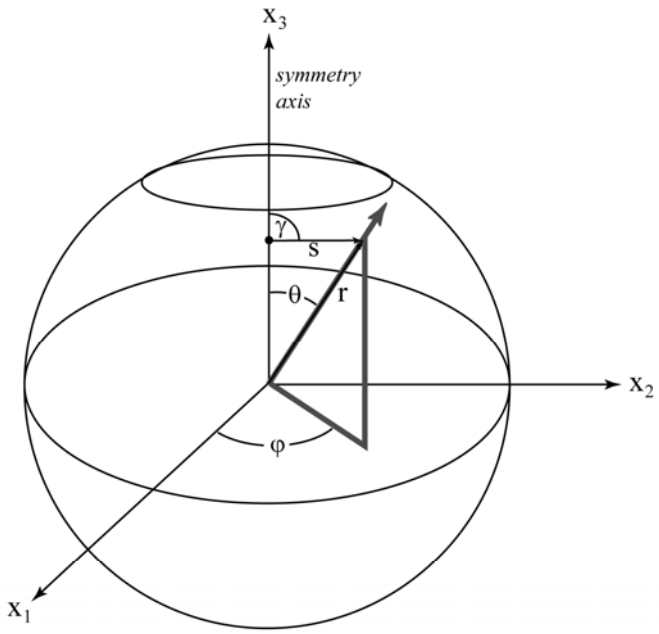


Figure 1.
(Jahnke, Thorne, Cochard, Igel 2007)
Span 1-column; black & white

Figure 1. Spherical coordinate system used in the formulation of the wave equation and the source description. All properties are invariant in the $\varphi$-direction. The distance from the Earth's center is denoted by $r$, and $\theta$ is the angular distance from the symmetry axis, $\gamma$ is the take-off angle, and $s$ is the source-receiver distance.

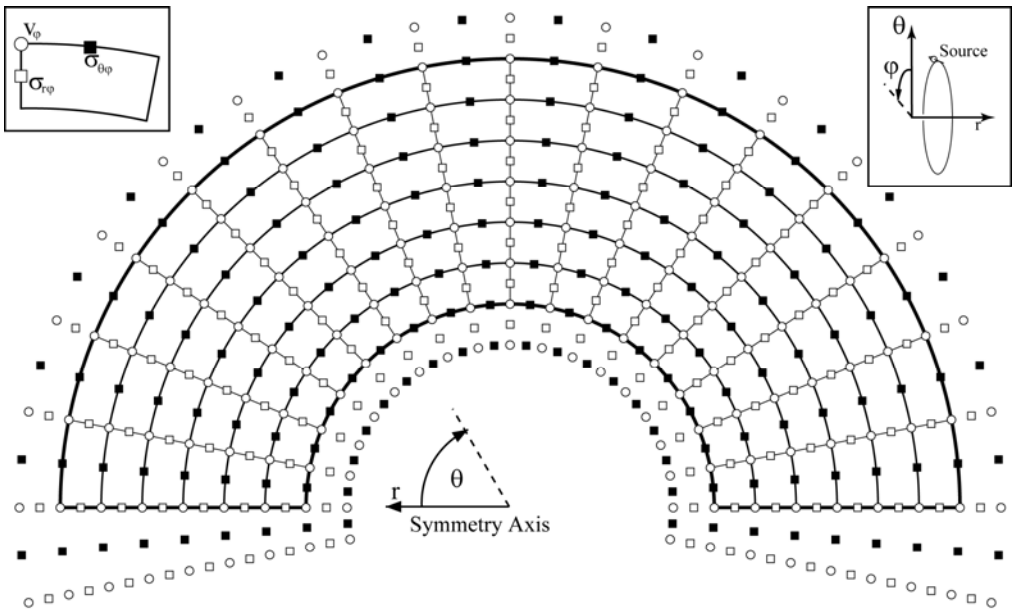


Figure 2.
(Jahnke, Thorne, Cochard, Igel 2007)
Span 2-columns; black & white

Figure 2. The staggered grid scheme used in the SHaxi algorithm. The origin of the coordinate system is placed at the Earth's center. The symmetry axis ($\theta$ = 0°) is horizontally aligned as labelled at the origin. The model boundaries (surface, CMB and symmetry axis) are framed with thick lines. The additional points outside the model space are used for implementation of the boundary conditions. The symbols representing the wave field properties $v_\varphi$, $\sigma_{r\varphi}$, and $\sigma_{\theta\varphi}$ are labelled in the unit grid-cell shown in the top left corner of the figure.

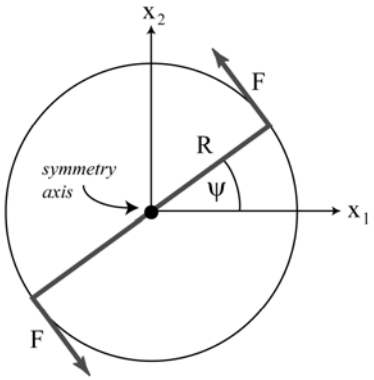


Figure 3.
(Jahnke, Thorne, Cochard, Igel 2007)
Span 1-column; black & white

Figure 3. Illustration of the ring source used in the SHaxi algorithm. The origin of the coordinate system corresponds to the symmetry axis. The ring source can be thought as a superposition of single forces F acting perpendicular to the radius vector R(ψ).

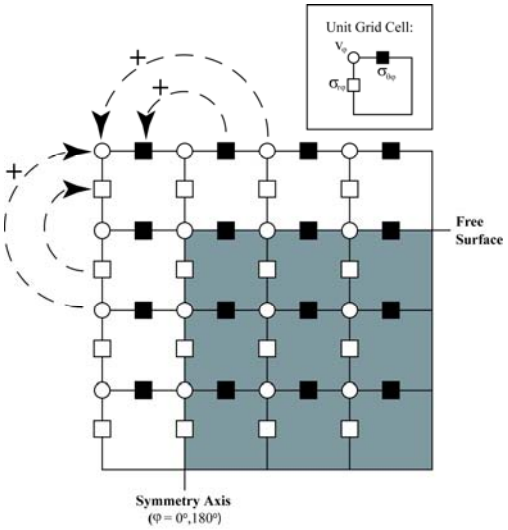


Figure 4.
(Jahnke, Thorne, Cochard, Igel 2007)
Span 1-column; black & white

Figure 4. Detail of the top-left corner of the SHaxi grid where the free surface and symmetry boundaries are encountered. The interior grid points (region underlain in gray) are part of the physical model space. To fulfill the boundary conditions, grid points

outside of the physical model space (region not underlain in gray) must be added to the total grid. These outer points are updated at each time step by corresponding values of grid elements inside the physical model space, as indicated by the arrows and the plus (+) and minus (-) symbols.

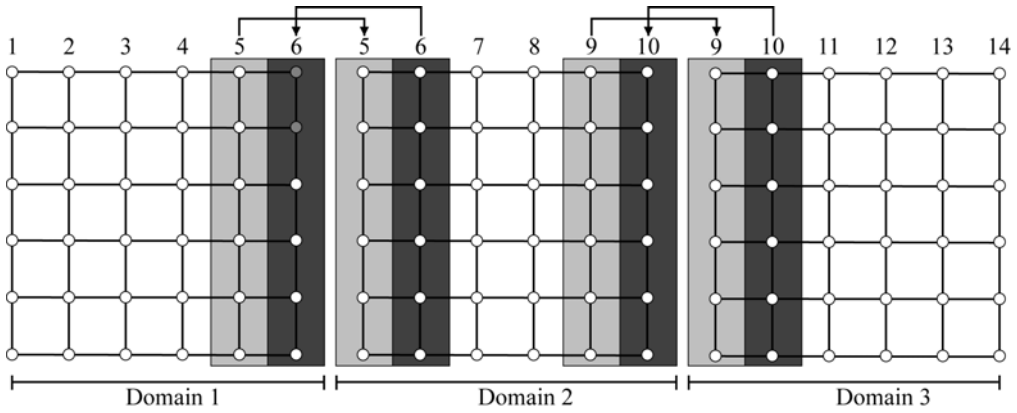


Figure 5.
(Jahnke, Thorne, Cochard, Igel 2007)
Span 2-columns; black & white

Figure 5. Schematic illustration of the domain decomposition used for parallelization of the SHaxi algorithm. The model space is divided into multiple domains (here shown for three domains) which are each processed by an individual node. After each time step the grid points at the boundaries of the domain (grid points underlain in gray) are copied to the corresponding grid points of the adjacent domain. The lateral size of the gray regions correspond to half the FD operator length.

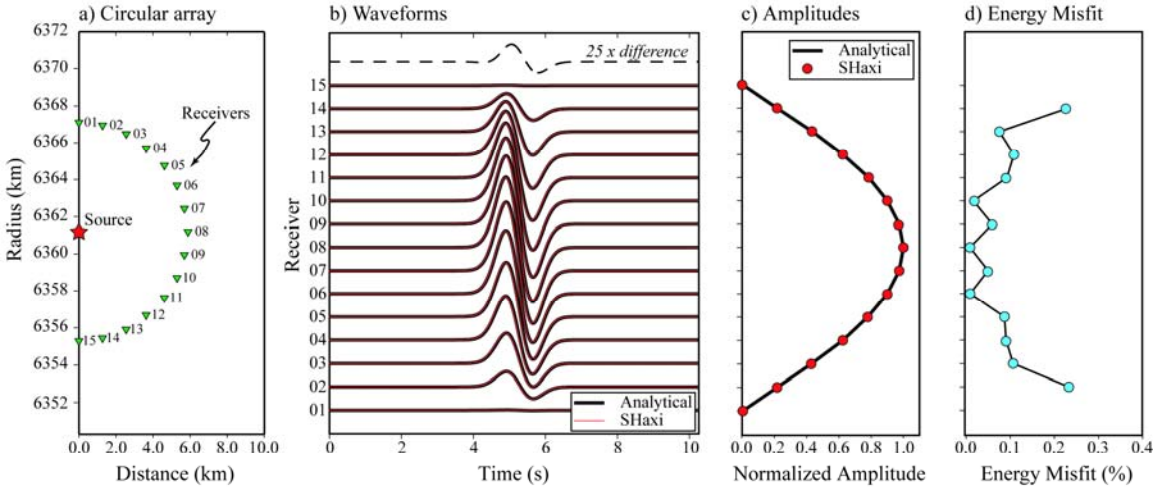


Figure 6.
(Jahnke, Thorne, Cochard, Igel 2007)
Span 2-columns; color

Figure 6. a) Source-receiver setup of the circular array used to examine the angular variation of the radiation pattern. In this setup the entire range of take-off angle is covered. b) Numerical FD (red solid line) and analytical (black solid line) seismograms for the array. The dashed line on top shows the difference trace for receiver no. 8 scaled by a factor of 25. c) The maximum FD amplitudes of all traces (red filled circles) are plotted on top of the analytical curve (solid line). d) The energy misfit of the FD solution with respect to the analytical solutions. Receivers 01 and 15 are on the nodal *SH* plane and the energy misfit is undefined. The energy misfit across all receivers is less than 0.3%.

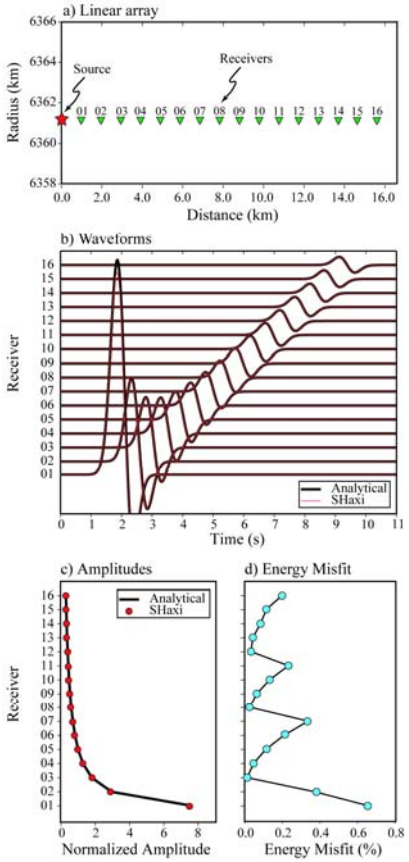


Figure 7.
(Jahnke, Thorne, Cochard, Igel 2007)
Span 1-column; color

Figure 7. a) Source-receiver setup of the linear array used to examine the geometrical spreading of the wave field. The receiver spacing corresponds to 0.6 dominant wavelengths (1.2 km) in the simulation. b) Numerical FD (red solid line) and analytical (black solid line) seismograms for the array. c) The maximum FD amplitudes of all traces (red filled circles) are plotted on top of the analytical curve (solid line). d) The energy misfit between the FD and analytical solutions. The misfit is below 0.8% for the entire section.

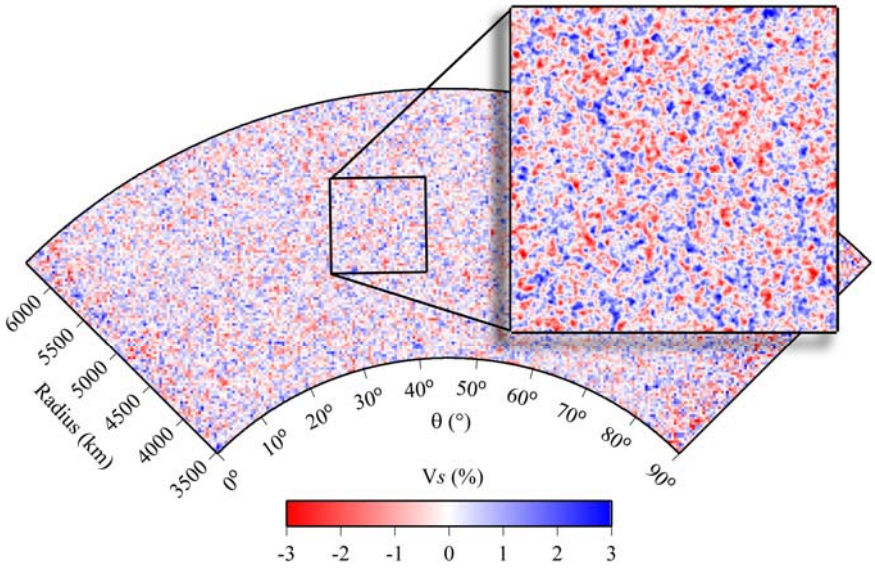


Figure 8.
(Jahnke, Thorne, Cochard, Igel 2007)
Span 2-columns; color

Figure 8. Example of SHaxi model for which random $V_S$ variations were applied to the PREM background model. In this example a Gaussian autocorrelation function was applied with a corner correlation length of 32 km. The RMS *S*-wave velocity perturbation is 1% and the maximum perturbation varies between ±3%. The left model boundary at $\theta$=0° is the symmetry axis.

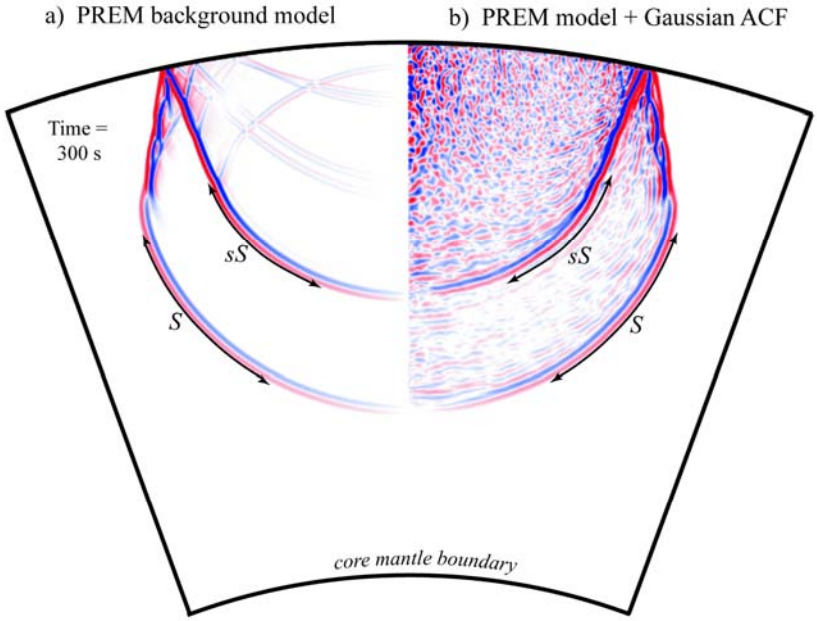


Figure 9.
(Jahnke, Thorne, Cochard, Igel 2007)
Span 2-columns; color

Figure 9. a) The *SH* velocity wavefield for a 200-km-deep source in the PREM background model at time = 300 s. The *S* and *sS* wave fronts are labeled. b) The velocity wave field at the same time step as in panel a) for the PREM model with random $V_S$ variations applied. The random variations were created with a Gaussian autocorrelation function with corner wavelength of 32 km and 3% RMS $V_S$ perturbations.

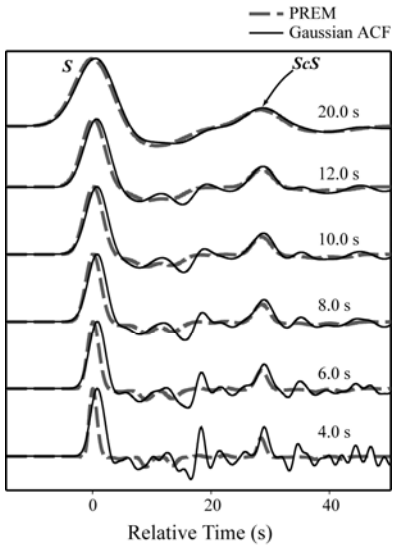


Figure 10.
(Jahnke, Thorne, Cochard, Igel 2007)
Span 1-column; black & white

Figure 10. Frequency dependence of scattering. Shown are SHaxi displacement seismograms for the PREM earth model (dashed line) compared to seismograms for a stochastically perturbed model with a Gaussian autocorrelation function created with a RMS VS perturbation of 3% and a 16 km corner correlation length superimposed on PREM (solid line). Each pair of seismograms has been filtered to a different dominant period listed directly above the seismogram pair. Seismograms are normalized to unity on the *S* arrival.

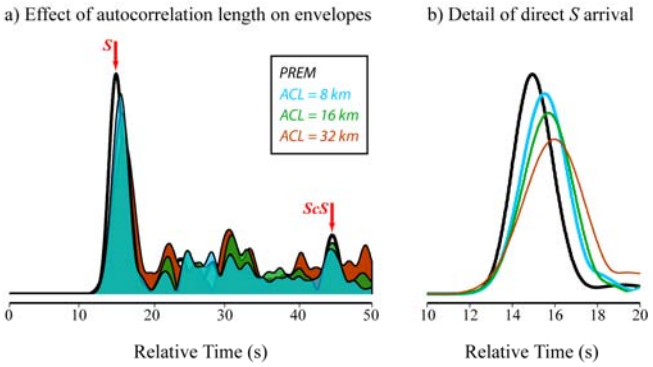


Figure 11.
(Jahnke, Thorne, Cochard, Igel 2007)
Span 2-columns; color

Figure 11. a) The dependence of autocorrelation length (ACL) on *SH*-wave envelopes. Envelopes of displacement seismograms are shown for the PREM model (black line) and for the PREM model with three realizations of random *S*-wave velocity perturbations applied. The perturbations are produced for a Gaussian autocorrelation function with 3% RMS velocity perturbations. Envelopes are shown for random perturbations with ACL's of 8 km (blue), 16 km (green) and 32 km (red). b) Detail of direct *S* arrival from panel a).

**Table 1. Example SHaxi parameters and performance – Linux Cluster.**

| Grid Size | | | | Number of Time Steps | Memory Usage[c] (Mb) | Dominant Period[d] (s) | | | | Run Time[e] |
|---|---|---|---|---|---|---|---|---|---|---|
| npts[a] (θ) | dθ[b] (km) | Npts (r) | dr (km) | | | *S* (40º) | *S* (80º) | *SS* (120º) | *SS* (160º) | |
| 5000/24 | 4.0/2.2 | 1000 | 2.9 | 16894 | 17 | 16 | 18 | 25 | 30 | 19 m |
| 10000/24 | 2.0/1.1 | 1800 | 1.6 | 33785 | 52 | 10 | 12 | 17 | 19 | 2 h 9 m |
| 15000/24 | 1.3/0.7 | 2900 | 1.0 | 50758 | 122 | 8 | 10 | 12 | 15 | 7 h 39 m |
| 20000/24 | 1.0/0.5 | 3800 | 0.76 | 67649 | 210 | 6 | 8 | 10 | 11 | 17 h 33 m |
| 30000/24 | 0.7/0.4 | 5200 | 0.55 | 101512 | 428 | 5 | 6 | 8 | 9 | 2 d 6 h 21 m |

[a]Values are: Total number of grid points / Number of processors used.
[b]Values are: dθ (at Earth surface) / dθ (at CMB)
[c]Memory is reported as total memory (code size + data size + stack size) for one processor. Code size is ~800 kb.
[d]Dominant Period based on phase and epicentral distance listed for a source depth of 500 km.
[e]Total run time is based on 2700.0s of simulation time.

**Table 2. Example SHaxi parameters and performance – "Iceberg" Supercomputer.**

| Grid Size[a] | | Number of Nodes[b] | Simulation Time = 1800 s | | Simulation Time = 2700 s | |
|---|---|---|---|---|---|---|
| npts (θ) | npts (r) | | Number of Time Steps | Run Time | Number of Time Steps | Run Time |
| 5000 | 1000 | 4 | 11281 | 13 m | 16921 | 21 m |
| 10000 | 1800 | 4 | 22560 | 1 h 31 m | 33840 | 2 h 16 m |
| 10000 | 1800 | 8 | 22560 | 57 m | 33840 | 1 h 24 m |
| 15000 | 2900 | 8 | 33838 | 3 h 2 m | 50758 | 4 h 24 m |
| 15000 | 2900 | 12 | 33838 | 2 h 20 m | 50758 | 3 h 32 m |
| 20000 | 3800 | 12 | 45099 | 5 h 46 m | 67649 | 8 h 14 m |
| 20000 | 3800 | 16 | 45117 | 4 h 30 m | 67676 | 6 h 23 m |
| 30000 | 5200 | 16 | 67675 | 12 h 26 m | 101512 | 17 h 38 m |

[a]Corresponding grid spacing is listed in Table 1.
[b]Each node consists of an IBM p655+ node, with 8 processors per node, and 16 Gb shared memory. Processor speed is 1.5 GHz.

**Table 3. Simulation parameters used in SHaxi verification.**

| Parameter | Linear Array | Circular Array |
|---|---|---|
| $V_S$ | 2000 m/s | 2000 m/s |
| Density (ρ) | 2000 kg/m$^3$ | 2000 kg/m$^3$ |
| dr | 77.5 m | 38.7 m |
| $Rd\theta$ | 48.9 m | 24.4 m |
| $T_{dom}$ | 1.0 s | 0.6 s |
| $\lambda_{dom}$ | 2000 m | 1200 m |
| Points per wavelength | 20 (radial) 40 (lateral) | |
| Receiver spacing | 976 m | 13.5° |
| Source-receiver distance | varies | 5859 m |